# 5 Noninvasive in vivo imaging using PET and BLI to monitor the biodistribution and function of tumor-targeted siRNA nanoparticles after intravenous injection in mice[†]

## 5.1 Abstract

Noninvasive in vivo imaging technologies can provide quantitative information about the spatiotemporal distribution and function of molecules in living organisms. Here, we demonstrate an approach using positron emission tomography (PET) and bioluminescent imaging (BLI) to quantify the in vivo biodistribution and function of nanoparticles formed with cyclodextrin-containing polycations (CDP) and small interfering RNA (siRNA). Conjugation of the metal chelator, 1,4,7,10-tetraazacyclododecane-1,4,7,10-tetraacetic acid (DOTA), to the 5' end of the siRNA molecules allows labeling with $^{64}$Cu for PET imaging. Since the siRNA molecules target luciferase, BLI of mice bearing luciferase-expressing Neuro2A subcutaneous tumors before and after PET imaging enabled correlation of functional efficacy with the biodistribution data. Both naked siRNA and siRNA packaged into nanoparticles showed rapid blood clearance with significant accumulation in the liver and kidneys. Despite the poor pharmacokinetics of the nanoparticle formulations, both non-targeted and transferrin (Tf)-targeted siRNA nanoparticles showed detectable tumor signal (~1% ID/cm$^3$) by PET 1 d post injection, and the Tf-targeted siRNA nanoparticles reduced luciferase activity by ~50% relative to non-targeted siRNA nanoparticles after 1 d. Therefore, the primary advantage of targeted nanoparticles may be associated with processes involved in cellular

[†] This work was performed in collaboration with Helen Su and Isabel Hildebrandt in the laboratory of Wolfgang A. Weber, Department of Molecular Medicine and Pharmacology, Jonsson Comprehensive Cancer Center, David Geffen School of Medicine, University of California at Los Angeles.

uptake rather than overall tumor localization. Moreover, we propose a physiologically based mechanism that could result in nanoparticle disruption primarily within the kidney, helping to explain the rapid blood clearance of the nanoparticles after systemic administration. This dissociation mechanism could have broad implications for the design of nucleic acid nanoparticles formed through electrostatic interactions and will likely facilitate the design of long-circulating nanoparticles.

## 5.2 Introduction

RNA interference (RNAi) is a powerful trigger of sequence-specific gene silencing, and its potential therapeutic use for treating diseases such as cancer is being widely investigated. Synthetic small interfering RNA (siRNA) molecules 19-21 bp in length can act as the mediators of RNAi if applied exogenously, but they must reach the intracellular environment to exert their effect. Therefore, therapeutic application of siRNAs requires their effective delivery into the target cells of interest. To address the challenge of nucleic acid delivery, a variety of approaches have been developed with varying success, including covalent attachment of antibodies or cholesterol, liposome encapsulation, or nanoparticle formation with cationic lipids or polymers (1-4). Nanoparticle encapsulation of siRNAs can help reduce renal clearance while adding features such as stabilization against nuclease degradation, tunable cell-specific targeting, and large payload delivery. We previously have described a cyclodextrin-containing polycation (CDP) and its interaction with siRNA to form targeted siRNA nanoparticles with diameters <100 nm that carry a payload of ~2,000 siRNA molecules (5). These nanoparticles have been used to deliver functional siRNA to tumors in vivo, inhibiting tumor growth in a disseminated model of Ewing's sarcoma (6). Importantly, these

nanoparticles show no clinical signs of toxicity in mice or non-human primates at the doses used for in vivo efficacy (7).

Recently, Medarova et al. described the use of MRI and fluorescence imaging to monitor the tumor accumulation and functional activity of magnetic nanoparticles covalently linked to siRNAs (8). This study illustrated the power of multimodality imaging approaches to help correlate the biodistribution of therapeutic entities with their biological activity. We attempt to extend this methodology further by employing microPET/CT to monitor the real-time, whole-body biodistribution kinetics and tumor localization of injected siRNA nanoparticles while concurrently using BLI to measure the luciferase knockdown by the delivered siRNA molecules. By formulating the nanoparticles with or without Tf targeting ligands, the effect of cell-specific targeting on both biodistribution and function can be studied.

A recent report by de Wolf et al. examined the effect of polycationic carriers on the pharmacokinetics and tumor localization of siRNA (9). They noted that formulation of the siRNA into polycationic carriers had little effect on the biodistribution and tumor localization compared to naked siRNA. Both naked siRNA and siRNA packaged into the carriers exhibited rapid blood clearance with tissue distribution mainly to the kidneys and liver within the first 15 minutes after injection.

In an extension of the aforementioned studies, we employ microPET/CT and BLI to determine the kinetics of the biodistribution and tumor localization of intravenously administered CDP-based siRNA nanoparticles while simultaneously quantifying the functional efficacy of the delivered siRNA molecules through luciferase reporter protein knockdown. This methodology represents a generalized procedure for studying any

siRNA-based carrier system in vivo, and we believe these results provide important insights into the design and optimization of nanoparticle carriers for systemic siRNA delivery.

## 5.3 Materials and methods

### *5.3.1 siRNA sequence*

To create the DOTA-modified siRNA, RNA oligonucleotides were ordered from Integrated DNA Technologies. The antisense strand (5'-UAUCGAAGGACUCUGGCACdTdT-3') was ordered unmodified. The sense strand (5'-GUGCCAGAGUCCUUCGAUAdTdT-3') was ordered unmodified or with a 5' Amino Modifier C6 modification to place an amine at the 5' end of this sense strand. The annealed siRNA duplex is designed to target luciferase mRNA.

### *5.3.2 Synthesis of DOTA-siRNA*

1,4,7,10-tetraazacyclododecane-1,4,7,10-tetraacetic acid mono(*N*-hydroxysuccinimide ester) (DOTA-NHS-ester) was ordered from Macrocyclics. The DOTA-NHS-ester reacts with the terminal amine on the amine-modified RNA sense strand to form a stable amide bond. To a microcentrifuge tube were added the RNA sense strand with a 100-fold molar excess of DOTA-NHS-ester in Chelex-100-treated carbonate buffer (pH 9). The contents were allowed to react with stirring for ~4 h at room temperature. The DOTA-RNAsense conjugate was ethanol precipitated with 0.1 volumes of 3M sodium chloride and 2.5 volumes of ethanol followed by incubation overnight at -20°C. The precipitation mixture was then centrifuged, washed with 70% ethanol, centrifuged again, and resuspended in water at a concentration of 1 mM. Finally, the purified DOTA-RNAsense was annealed to the unmodified antisense strand to yield

DOTA-siRNA. All liquids were pre-treated with Chelex-100 (Bio-Rad) to remove trace metal contaminants.

### *5.3.3 Verification of DOTA-siRNA conjugation*

To verify successful conjugation of DOTA to siRNA, a procedure was designed to compare the ability of DOTA-siRNA to coordinate gadolinium ($Gd^{3+}$) relative to free DOTA. To a microcentrifuge tube were added equimolar amounts of gadolinium chloride ($GdCl_3$) and either DOTA or DOTA-siRNA in 0.1 M ammonium acetate buffer (pH 6). The microcentrifuge tubes were incubated for 15 min at 75°C for the labeling reaction. Subsequently, half of the labeling reaction was combined with an equal volume of 1 mM arsenazo III. The presence of any free gadolinium ions results in a hypochromic shift from 548 nm to 660 nm. Therefore, the absorbance at 660 nm was measured for each sample using a Tecan Safire plate reader. Comparison to a standard curve allowed estimation of the amount of free gadolinium remaining in each sample.

### *5.3.4 In vitro transfection*

Neuro2A-Luc cells with constitutive luciferase expression were seeded at $2x10^4$ cells per well in 24-well plates 2 days prior to transfection and grown in DMEM supplemented with 10% FBS and antibiotics (penicillin/streptomycin). siRNA was complexed with Oligofectamine (Invitrogen) according to manufacturer's instructions and applied to each well in a total volume of 200 μL Opti-MEM I (Invitrogen). Transfection media was removed and replaced with complete media after 5 h. The kinetics of the luciferase knockdown by unmodified and DOTA-conjugated siRNA were determined using the Xenogen IVIS 100 as described previously (10).

### *5.3.5 $^{64}$Cu labeling of DOTA-siRNA*

$^{64}$Cu chloride was produced at Washington University (St. Louis, MO). Upon arrival, the $^{64}$Cu chloride was mixed with 0.25 M ammonium acetate (pH 7) and transferred to a new microcentrifuge tube. Citrate buffer (pH 5) was added to this microcentrifuge tube to achieve a final concentration of 0.1 M citrate buffer. DOTA-siRNA in water was added to achieve a final DOTA-siRNA:$^{64}$Cu ratio of 250:1 for labeling. The contents of the tube were mixed and then allowed to sit for 1 h at 60°C. The labeling reaction was purified by gel filtration or ethanol precipitation. Gel filtration was performed using MicroSpin G-25 columns (Amersham Biosciences) according to manufacturer's instructions. Ethanol precipitation was accomplished by adding 0.1 volumes of 3M sodium acetate and 2.5 volumes of pre-chilled ethanol followed by incubation for ~2 h at -80°C. The precipitation reaction was then centrifuged to pellet the DOTA-siRNA, washed with 70% ethanol, centrifuged again, and resuspended in water to yield $^{64}$Cu-DOTA-siRNA.

### *5.3.6 Nanoparticle formation*

Before addition to the nucleic acid, the CDP was mixed with AD-PEG at a 1:1 AD-PEG:β-CD (mol:mol) ratio in water. Targeted nanoparticles contained AD-PEG-transferrin (AD-PEG-Tf) as a percentage of the total AD-PEG in the mixture. For example, 1 mol% AD-PEG-Tf nanoparticles contained 0.01 moles AD-PEG-Tf for every 0.99 moles AD-PEG, and 0.1 wt% AD-PEG-Tf nanoparticles contained 0.001 g of AD-PEG-Tf for every 1 g of AD-PEG. The mixture of CDP, AD-PEG, and AD-PEG-Tf in water was then added to an equal volume of siRNA (or a mixture of unmodified siRNA and DOTA-siRNA) in water such that the ratio of positive charges from CDP to negative

charges from the nucleic acid was equal to the desired charge ratio of 3 (+/-). An equal volume of 10% (w/v) glucose in water was added to the resulting nanoparticles to give a final concentration of 5% (w/v) glucose suitable for injection.

### *5.3.7 Dynamic light scattering (DLS)*

Nanoparticle formulations were diluted to a volume of ~1.5 mL, placed in a cuvette, and inserted into a ZetaPALS (Brookhaven Instruments Corporation) instrument to measure both the size and zeta potential. Reported effective hydrodynamic diameters represent the average values from a total of 5-10 runs of 30 seconds each, while zeta potentials represent the average of 10 runs each.

### *5.3.8 Serum stability of siRNA nanoparticles*

Nanoparticles were formed in water at a charge ratio of 3 (+/-) with an siRNA concentration of 0.5 g/L, and subsequently incubated in 50% mouse serum (Sigma) for 4 h at 37°C and 5% $CO_2$. Aliquots of the nanoparticles were removed at the specified time points (1 h, 4 h, 17 h, 43 h) and run on an agarose gel to determine the amount of intact siRNA remaining. Nanoparticles that were incubated in water instead of mouse serum were loaded as controls for each gel. Displacement of the nucleic acid from the nanoparticles was achieved by adding 1% sodium dodecyl sulfate (SDS) to the sample immediately prior to gel loading. Gel electrophoresis was performed by applying 100 V for 30 min, and the siRNA bands were visualized by ethidium bromide staining. Quantification of the band intensities was accomplished using ImageJ software.

### *5.3.9 Salt stability of siRNA and pDNA nanoparticles*

Nanoparticles were formulated as described above with a 1:1 AD-PEG:β-CD (mol:mol) ratio and a charge ratio of 3 (+/-). Nanoparticles were formed at an siRNA or

pDNA concentration of 0.5 g/L. A portion of the nanoparticle formation (containing 1 μg siRNA) was added to a microcentrifuge tube and mixed with either 1% SDS or sodium chloride (NaCl) at a range of concentrations from 0 to 1.5 M NaCl. The samples were allowed to incubate for 3-5 min at room temperature before being loaded into a 1% agarose gel. Gel electrophoresis was performed by applying 100 V for 30 min (siRNA nanoparticles) or 80 V for 60 min (pDNA nanoparticles), and the bands were visualized by ethidium bromide staining. Quantification of the amount of siRNA or pDNA present in intact nanoparticles (remaining in the well at the top of the gel) was performed using ImageJ image analysis software.

### *5.3.10 Animals and tumor formation*

Severe combined immunodeficient (NOD/scid) mice were purchased from Jackson Laboratories. All animal manipulations were performed with sterile technique following the guidelines of the UCLA Animal Research Committee. Neuro2A-Luc cells were cultured in DMEM supplemented with 10% FBS, 2 mg/mL glucose, 100 units/mL of penicillin, and 100 units/mL of streptomycin. Exponentially growing Neuro2A-Luc cells were removed from the plate with trypsin, resuspended in PBS and Matrigel (BD Biosciences), and injected subcutaneously into the right flank of NOD/scid mice at 1-$2x10^6$ cells per mouse. Animals underwent microPET/CT scanning after tumors had grown to an approximate size of 6-7 mm in diameter.

### *5.3.11 MicroPET/CT imaging*

MicroPET/CT imaging was performed with a microPET FOCUS 220 PET scanner (11) (Siemens Preclinical Solutions) and MicroCAT II CT scanner (Siemens Preclinical Solutions). Mice were placed on a heating pad (30°C) and anesthetized using

1.5-2% isoflurane starting 15 min prior to injection. 3.7-11.1 MBq (100-300 μCi) of $^{64}$Cu was injected via tail vein while the animals were positioned on the scanner bed before a dynamic PET study was acquired for one hour. Mice were then placed in an imaging chamber that minimizes positioning errors between PET and CT to less than 1 mm (11). PET images were reconstructed by filtered back projection, using a ramp filter to yield an image resolution of 1.7 mm. Immediately after the PET scan, mice underwent a 7-minute microCT scan, using routine image acquisition parameters (11). The microCT scan was used for anatomical localization of the tissue concentrations of the $^{64}$Cu over time in the microPET study. Static PET scans were acquired the following day (~18-24 h after the initial injection) with another CT scan for anatomical co-registration.

To determine temporal changes of tracer concentration in various organs, elliptical regions of interest (ROI) were placed in the area of the organ that exhibited the highest $^{64}$Cu activity as determined by visual inspection. To ensure accurate anatomical positioning of the ROIs in the various organs, ROIs were placed on fused microPET/CT images generated by the AMIDE software (12). Activity concentrations are expressed as percent of the decay-corrected injected activity per cm$^3$ of tissue (can be approximated as %ID/g) using the AMIDE software. The activity in each ROI over time is reported as the percent of the decay-corrected injected activity per cm$^3$ (%ID/cm$^3$), and these values were normalized to an elliptical cylinder ROI drawn over the entire mouse to correct for the actual injected activity.

### *5.3.12 Bioluminescent imaging (BLI)*

Bioluminescent imaging was performed using a Xenogen IVIS 100 imaging system. Mice were anesthetized with 2.5% isoflurane and injected i.p. with 0.2 mL of a

15 g/L D-luciferin solution in PBS. Light emission was measured 10 minutes after injection of the D-luciferin solution, and bioluminescent signals were quantified using Living Image software (Xenogen,).

## 5.4 Results

### *5.4.1 Synthesis and characterization of DOTA-siRNA*

To verify conjugation of DOTA to the siRNA, a non-radioactive assay was designed to quantify the relative ability of DOTA-siRNA and free DOTA to coordinate gadolinium. Incubation with DOTA-siRNA typically yielded gadolinium binding efficiencies that were about 50% of that observed for free DOTA.

Since the DOTA-siRNA is also designed to target the luciferase mRNA, its ability to silence luciferase expression in luciferase-expressing cell lines was compared to that of unmodified siRNA against luciferase (Figure 5.1). While the unmodified siRNA is able to achieve a maximum luciferase knockdown of >75%, the DOTA-siRNA achieves about 50% maximum luciferase knockdown, indicating a slight loss in activity after DOTA conjugation. Furthermore, the duration of the knockdown is consistent with an RNAi-based mechanism (10).

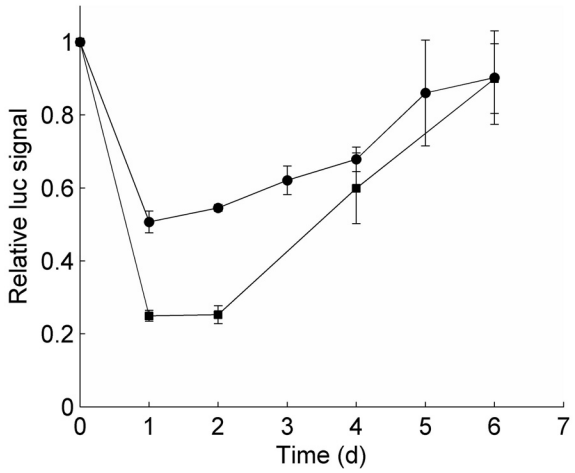


Figure 5.1. Luciferase knockdown by unmodified and DOTA-conjugated siRNA in luciferase-expressing Neuro2A-Luc cells. Luciferase knockdown is reported relative to the luciferase activity from cells transfected with equal doses of the siCON control sequence. Circles = DOTA-siRNA, squares = unmodified siRNA. Error bars = *SD*.

### *5.4.2 Formation of nanoparticles containing DOTA-siRNA*

Since conjugation of DOTA to the siRNA molecules may interfere with nanoparticle assembly, dynamic light scattering and gel electrophoresis were used to analyze the nanoparticles formed with DOTA-siRNA. The fraction of the total siRNA that is modified with DOTA has a negligible effect on nanoparticle zeta potential and only a minor effect on nanoparticle size, leading to a slightly larger hydrodynamic diameter as the fraction of DOTA-siRNA is increased (Figure 5.2). Gel electrophoresis shows that nanoparticles formed with or without DOTA-siRNA have similar migration patterns, and the majority of the siRNA (unmodified or DOTA-conjugated) remains bound within the nanoparticles after formation.

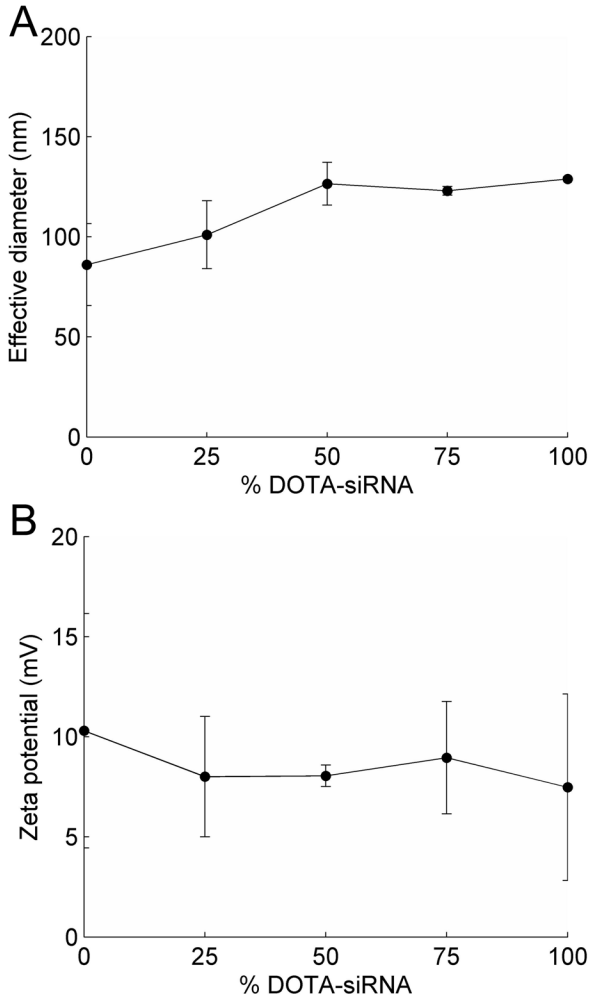


Figure 5.2. Effective hydrodynamic diameter (A) and zeta potential (B) of nanoparticles formed with 0 to 100% DOTA-siRNA. Error bars = *SD*.

### *5.4.3 $^{64}$Cu-labeling of DOTA-siRNA*

After labeling the DOTA-siRNA with $^{64}$Cu, purification was accomplished using one of two methods: gel filtration or ethanol precipitation. Aliquots of $^{64}$Cu-DOTA-siRNA purified by the two methods were separated by gel electrophoresis and the amount of radioactivity in the bands was quantified by a gamma counter. Relative to the total amount loaded per well, 95% and 90% of the radioactivity was associated with the siRNA band for the $^{64}$Cu-DOTA-siRNA purified by gel filtration and ethanol precipitation, respectively. Estimation of the overall yield of the recovery was made

using ImageJ analysis of the band intensities, indicating the total amount of siRNA recovered instead of the fraction of the radioactivity in the purification reaction associated with the DOTA-siRNA. According to the relative band intensities, close to 90% of the initial siRNA in the labeling reaction was recovered after ethanol precipitation, whereas only about 30% of the siRNA was recovered after gel filtration.

### *5.4.4 Serum stability of DOTA-siRNA nanoparticles*

Nanoparticles were formed with unmodified siRNA or with DOTA-siRNA representing either 20% or 50% of the total siRNA in the nanoparticles. These nanoparticles were then incubated in 50% mouse serum for 1 to 43 hours and analyzed by gel electrophoresis. The total amount of siRNA (unmodified or DOTA-conjugated) remaining at each time point was quantified by ImageJ analysis of the relative band intensities. All three types of nanoparticles demonstrated essentially equivalent stability against nuclease degradation of the encapsulated siRNA, with an estimated half-life of ~11 h (Figure 5.3). This indicates that the nanoparticle formulations do provide stabilization against siRNA nuclease degradation, since the naked siRNA duplexes degrade in mouse serum with a half-life of approximately 1 h (13).

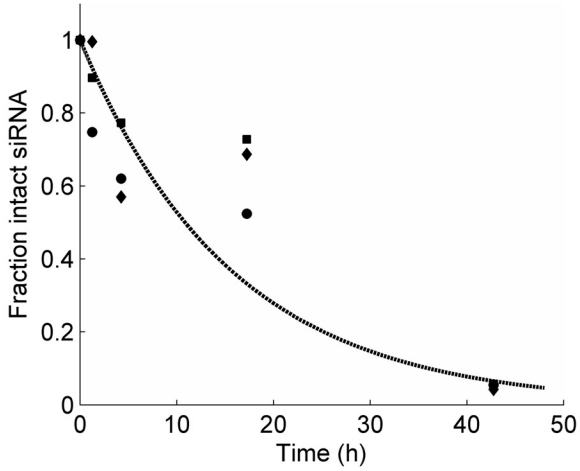


Figure 5.3. Nuclease stability of nanoparticle-encapsulated siRNA after incubation at 37°C and 5% $CO_2$ in 50% mouse serum. After gel electrophoresis, band intensities were quantified with ImageJ software and plotted versus time to estimate the degradation half-life of the encapsulated siRNA. Circles = nanoparticles formed with unmodified siRNA, diamonds = nanoparticles formed with 20% DOTA-siRNA, squares = nanoparticles formed with 50% DOTA-siRNA.

### *5.4.5 Biodistribution of naked siRNA and siRNA nanoparticles after intravenous administration*

MicroPET/CT was used to examine the kinetics of the biodistribution and tumor localization of $^{64}$Cu-labeled molecules after intravenous injection in mice. Reconstructed microPET/CT images of mice at 1, 10, and 60 min after injection are shown in Figure 5.4. The images were quantified using AMIDE software and the %ID/cm$^3$ was calculated for each ROI over all time frames. The resulting time-activity curves shown in Figure 5.5 represent the averages from 2 ($^{64}$Cu, $^{64}$Cu-DOTA) or 3 ($^{64}$Cu-DOTA-siRNA ,Tf-targeted nanoparticles) independent experiments.

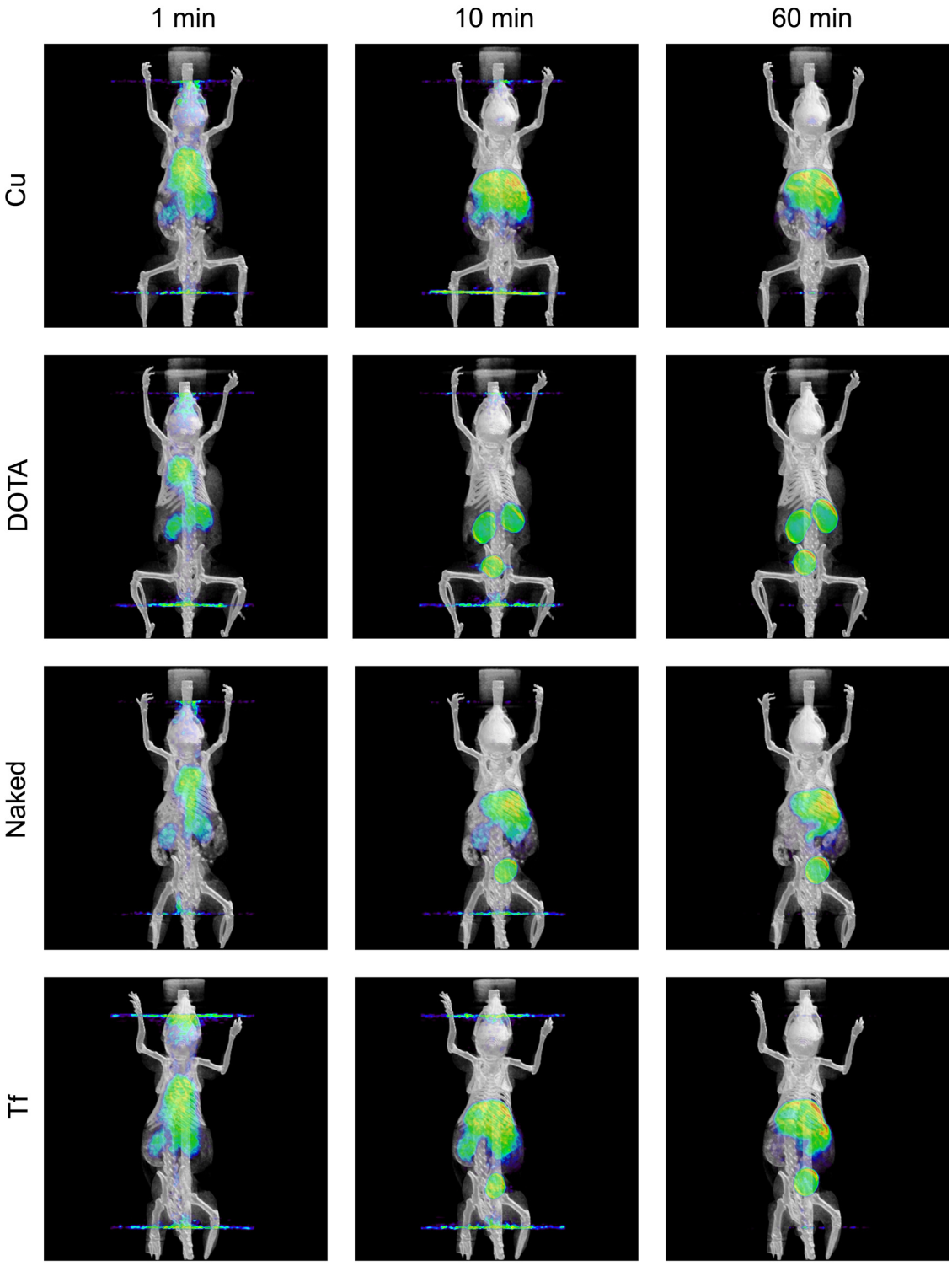


Figure 5.4. Fused microPET/CT images of mice at 1, 10, and 60 min after intravenous injection of free $^{64}$Cu (Cu), $^{64}$Cu-labeled DOTA (DOTA), $^{64}$Cu-labeled DOTA-siRNA (Naked), and Tf-targeted nanoparticles (Tf) containing ~50% $^{64}$Cu-labeled DOTA-siRNA. All images are displayed on the same scale (min threshold = 1 %ID/cm$^3$, max threshold = 5 %ID/cm$^3$).

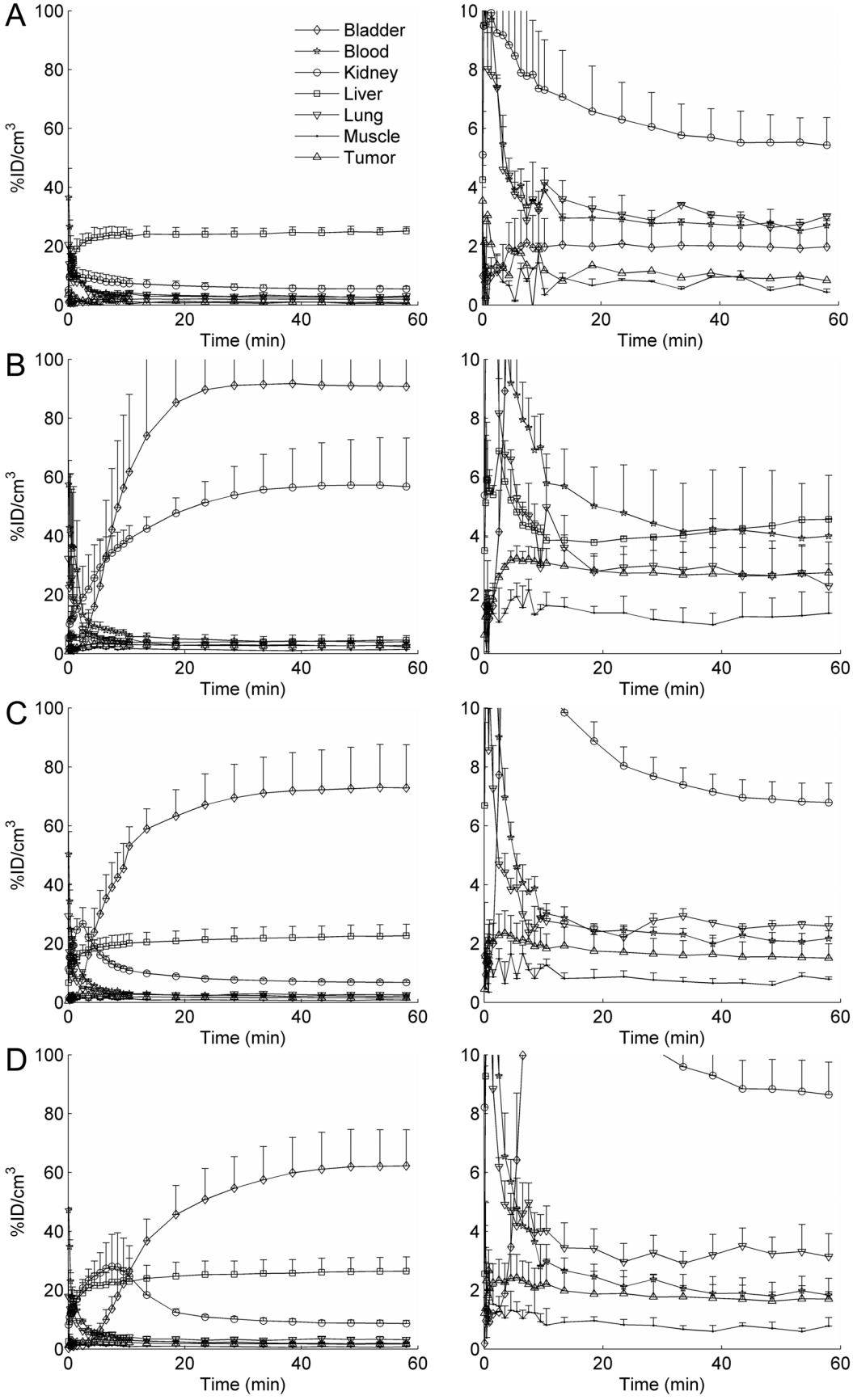
A
B
C
D
Bladder
Blood
Kidney
Liver
Lung
Muscle
Tumor
%ID/cm3
Time (min)

Figure 5.5. Average time-activity curves for the first 60 min after intravenous injection of (A) $^{64}$Cu, (B) $^{64}$Cu-labeled DOTA, (C) $^{64}$Cu-labeled DOTA-siRNA, and (D) Tf-targeted nanoparticles containing ~50% $^{64}$Cu-labeled DOTA-siRNA. Regions of interest (ROI) were drawn within each tissue or organ and the %ID/cm$^3$ for each ROI was calculated over all time frames using AMIDE software. Error bars = *SE*.

$^{64}$Cu alone accumulates rapidly in the liver, likely a result of binding to serum proteins such as albumin or ceruloplasmin (14). However, when the $^{64}$Cu is chelated by DOTA and injected systemically in mice, the majority of the injected dose rapidly enters the kidney, with some clearing to the bladder. This importantly shows that the $^{64}$Cu is not released by the DOTA in the serum, since any free $^{64}$Cu would rapidly accumulate in the liver. These results are also consistent with the kidney clearance of other metal chelators, such as DTPA (15). When the DOTA is conjugated to an siRNA molecule and labeled with $^{64}$Cu ($^{64}$Cu-DOTA-siRNA), the tissue distribution is different from either the $^{64}$Cu alone or the $^{64}$Cu-DOTA, with biodistribution kinetics characterized by rapid blood clearance resulting from both liver accumulation and kidney filtration into the urine. The total siRNA administered per mouse was equal to 2.5 mg/kg, and this $^{64}$Cu-DOTA-siRNA was purified by ethanol precipitation. Since the labeling efficiency for the DOTA-siRNA was approximately 30-50%, the fraction of DOTA-siRNA [DOTA-siRNA/(DOTA-siRNA+normal siRNA)] was around 50%. The plasma concentration of the $^{64}$Cu-DOTA-siRNA was fit using a biexponential decay with an initial elimination half-life of 1.8 min and a terminal elimination half-life of 61.9 min. The rapid initial elimination half-life is expected for the siRNA molecules whose small size (~13 kDa) allows first-pass renal clearance. Previously, Soutschek et al. reported an siRNA plasma half-life of ~6 min, consistent with the short half-life observed here (1). Additionally, Braasch et al. observed that intravenously injected siRNA accumulated in the kidney and

liver, with a peak in the kidney concentration 5 min after injection (16). Again, these observations are consistent with the values obtained here using microPET.

microPET/CT was also used to examine the kinetics of the biodistribution and tumor localization of siRNA nanoparticles after intravenous injection in mice. Given that the total dose of siRNA within the nanoparticles was the same as that used for naked siRNA (2.5 mg/kg), the fraction of DOTA-siRNA [DOTA-siRNA/(DOTA-siRNA+normal siRNA)] was still approximately 50%. The biodistribution of the $^{64}$Cu-DOTA-siRNA packaged into the Tf-targeted nanoparticles appears very similar to that observed for naked $^{64}$Cu-DOTA-siRNA, except the nanoparticle formulation led to slightly higher liver accumulation and a delayed peak in kidney activity.

The significant portion of the activity for the Tf-targeted nanoparticles that cleared rapidly through the kidneys and was excreted in the urine indicates the possibility of the presence of free siRNA. To investigate whether the free siRNA was present before injection, the nanoparticle formulations were analyzed by gel electrophoresis immediately before injection (Figure 5.6). The nanoparticle formulations showed <10% free siRNA when analyzed on the gel (Lanes 3 and 5 of Figure 5.6), and this small amount of free siRNA could also be an artifact from the gel electrophoresis procedure. Moreover, the slight decrease in the amount of migrating free siRNA at higher formulation charge ratios did not change the patterns of the time-activity curves after microPET/CT imaging. This supports the notion that any residual free siRNA prior to injection is not the dominant factor contributing to the kidney and bladder activity for the nanoparticle formulations. The urine was collected from mice injected with the siRNA nanoparticles and analyzed by agarose gel electrophoresis to further investigate whether

the activity observed in the kidney and bladder was associated with intact siRNA molecules (Figure 5.7). Visual inspection of the gel reveals a distinct band at the position corresponding to the migration distance of free siRNA (Lane 5 of Figure 5.7); however, a faint band is also seen at this same position for urine from mice that were not injected with any siRNA (Lane 8 of Figure 5.7). Subsequently, each lane was cut into four pieces (top, upper mid, lower mid, bottom) and a gamma counter was used to quantify the radioactivity in each region. At 30 min post injection, ~20% of the total radioactivity loaded into the lane was associated with the region corresponding to the migration distance of intact siRNA. This indicates that intact $^{64}$Cu-DOTA-siRNA may be responsible for at least a portion of the observed kidney and bladder activity.

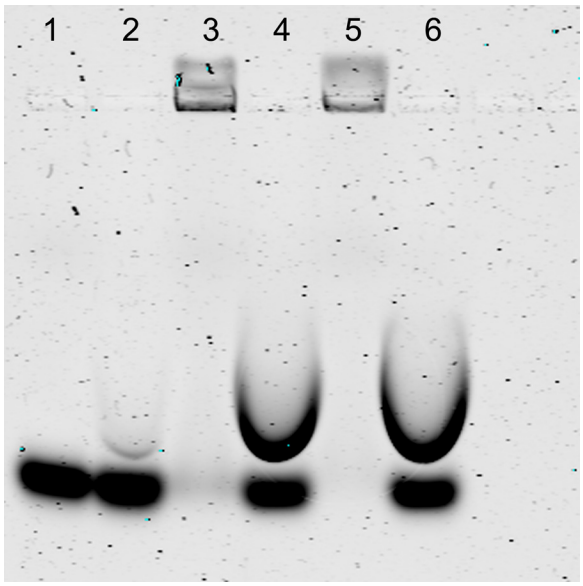


Figure 5.6. Gel electrophoresis analysis of $^{64}$Cu-DOTA-siRNA nanoparticles prior to injection for microPET/CT imaging. Lane 1 = $^{64}$Cu-DOTA-siRNA in water, Lane 2 = $^{64}$Cu-DOTA-siRNA + 1% SDS in water, Lane 3 = $^{64}$Cu-DOTA-siRNA packaged into Tf-targeted nanoparticles (charge ratio (+/-) = 3), Lane 4 = $^{64}$Cu-DOTA-siRNA packaged into Tf-targeted nanoparticles (charge ratio (+/-) = 3) + 1% SDS, Lane 5 = $^{64}$Cu-DOTA-siRNA packaged into Tf-targeted nanoparticles (charge ratio (+/-) = 6), Lane 6 = $^{64}$Cu-DOTA-siRNA packaged into Tf-targeted nanoparticles (charge ratio (+/-) = 6) + 1% SDS.

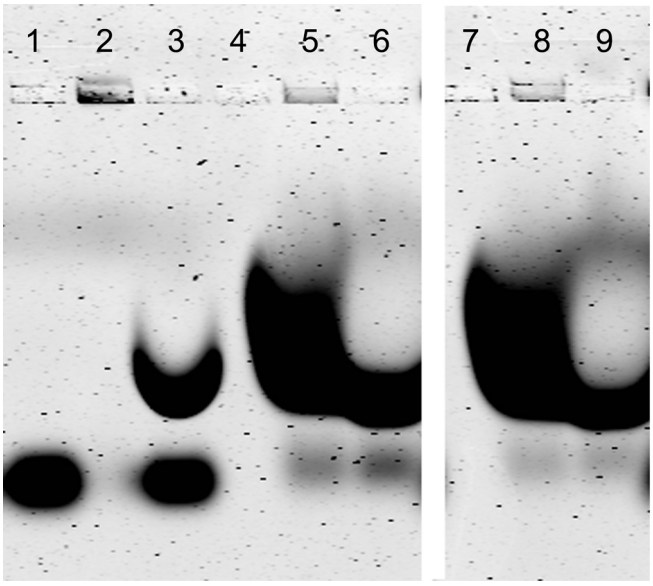


Figure 5.7. Gel electrophoresis analysis of urine samples from mice injected with $^{64}$Cu-DOTA-siRNA nanoparticles. Lane 1 = Naked unmodified siRNA in water, Lane 2 = $^{64}$Cu-DOTA-siRNA packaged into Tf-targeted nanoparticles (charge ratio (+/-) = 3), Lane 3 = $^{64}$Cu-DOTA-siRNA packaged into Tf-targeted nanoparticles (charge ratio (+/-) = 3) + 1% SDS, Lane 4 = empty, Lane 5 = 20 μL urine from a mouse injected with $^{64}$Cu-DOTA-siRNA packaged into Tf-targeted nanoparticles (charge ratio (+/-) = 3), Lane 6 = 20 μL urine from a mouse injected with $^{64}$Cu-DOTA-siRNA packaged into Tf-targeted nanoparticles (charge ratio (+/-) = 3) + 1% SDS, Lane 7 = empty, Lane 8 = 20 μL urine from an untreated mouse, Lane 9 = 20 μL urine from an untreated mouse + 1% SDS.

In an attempt to elucidate a possible physiologically based mechanism for the nanoparticle dissociation and release of free siRNA after intravenous administration, gel electrophoresis was used to examine the stability of the nanoparticles against dissociation when incubated in physiological salt (NaCl) concentrations. As shown in Figure 5.8, incubation of the nanoparticles with increasing salt concentration from 0 to 1.5 M NaCl led to a decrease in the intensity of the band at the top of the gel (siRNA within nanoparticles) with a corresponding increase in the intensity of the bands corresponding to free siRNA (an apparent shift in mobility for free siRNA appears to occur at salt concentrations above ~1 M). Since the nanoparticles are formed by electrostatic interactions between the positively charged cationic polymer strands and the negatively charged siRNA molecules, high salt concentrations can weaken these interactions and

allow release of free siRNA. This salt-mediated disruption of the nanoparticles would be consistent with the slight delay in peak kidney activity observed for the nanoparticle formulations relative to naked siRNA. Such a delay would be indicative of the dissociation of the nanoparticles leading to release of the free siRNA that is then rapidly cleared by the kidneys. When the same experiment was conducted using pDNA instead of siRNA as the nucleic acid, the nanoparticles were not as easily disrupted by the presence of NaCl (Figure 5.8). These results indicate that the siRNA nanoparticles are more susceptible to salt-mediated disruption than pDNA nanoparticles, perhaps owing to the smaller polyanion size for the siRNA relative to plasmid DNA.

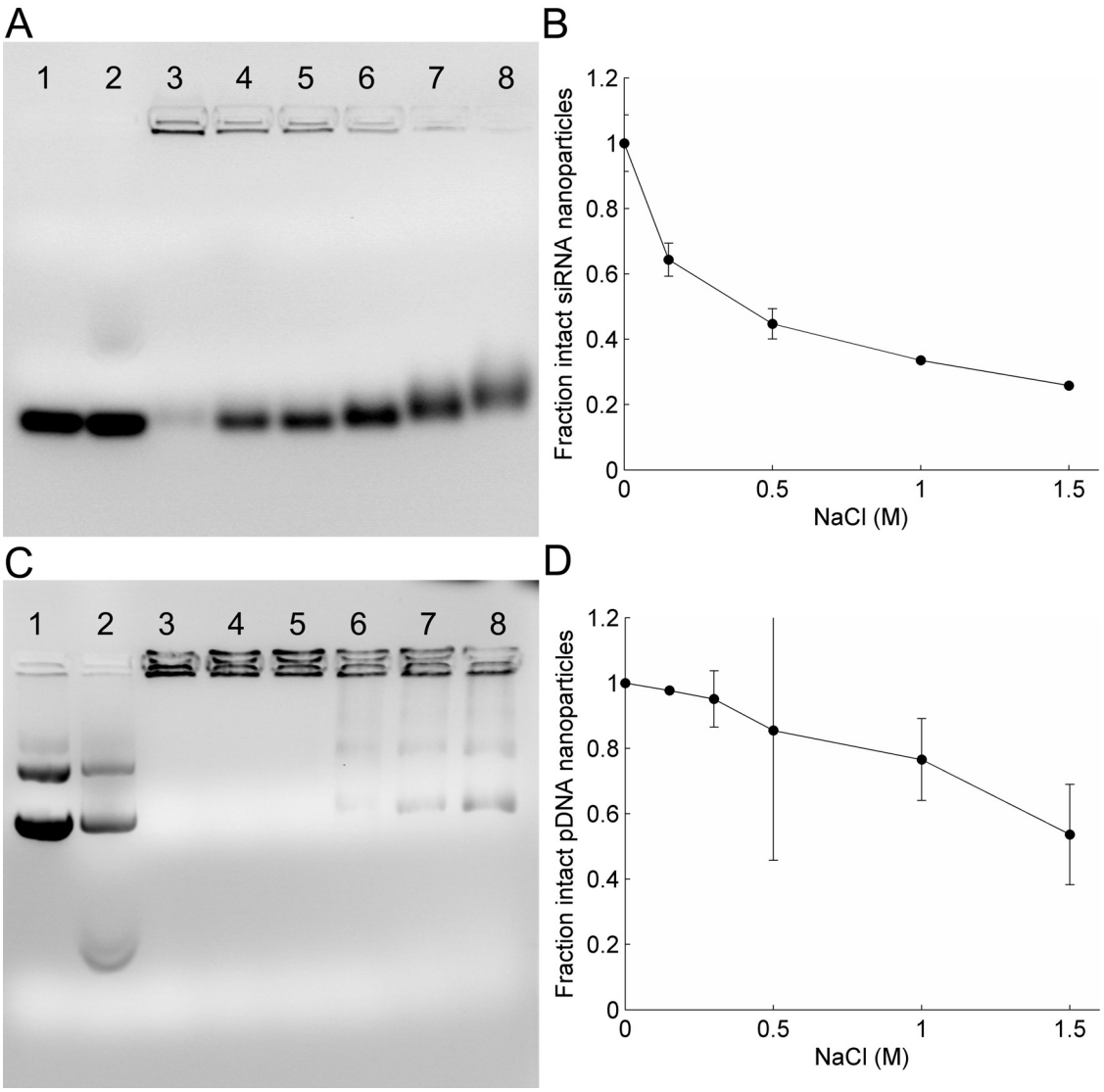


Figure 5.8. NaCl concentration-dependent disruption of Tf-targeted nanoparticles containing unmodified siRNA or pDNA. (A) Gel electrophoresis of siRNA nanoparticles: Lane 1 = naked siRNA, Lane 2 = nanoparticles + 1% SDS, Lane 3 = nanoparticles in water, Lane 4 = nanoparticles in 1X PBS, Lane 5 = nanoparticles in 0.15 M NaCl, Lane 6 = nanoparticles in 0.5 M NaCl, Lane 7 = nanoparticles in 1 M NaCl, Lane 8 = nanoparticles in 1.5 M NaCl. (B) Fraction of intact siRNA nanoparticles based on intensity in the wells (corresponding to siRNA within intact nanoparticles). The change in intensity with increasing NaCl concentration was normalized to the intensity for siRNA nanoparticles incubated in water alone (Lane 3). Error bars = *SD*. (C) Gel electrophoresis of pDNA nanoparticles: Lane 1 = naked pDNA, Lane 2 = nanoparticles + 1% SDS, Lane 3 = nanoparticles in water, Lane 4 = nanoparticles in 0.15 M NaCl, Lane 5 = nanoparticles in 0.3 M NaCl, Lane 6 = nanoparticles in 0.5 M NaCl, Lane 7 = nanoparticles in 1 M NaCl, Lane 8 = nanoparticles in 1.5 M NaCl. (D) Fraction of intact pDNA nanoparticles based on intensity in the wells (corresponding to pDNA within intact nanoparticles). The change in intensity with increasing NaCl concentration was normalized to the intensity for pDNA nanoparticles incubated in water alone (Lane 3).

### *5.4.6 Tumor localization and function of targeted vs. non-targeted siRNA nanoparticles*

A multimodality imaging approach was taken to investigate the biodistribution and functional activity of siRNA delivered by Tf-targeted or non-targeted nanoparticles. MicroPET/CT was used to analyze the biodistribution and tumor localization of the siRNA nanoparticles, while BLI enabled quantification of the luciferase knockdown by the delivered siRNA against luciferase. The tissue distribution of the $^{64}$Cu-DOTA-siRNA delivered by Tf-targeted and non-targeted nanoparticles was very similar for the first hour after injection, with similar blood clearance and tumor accumulation (Figure 5.9).

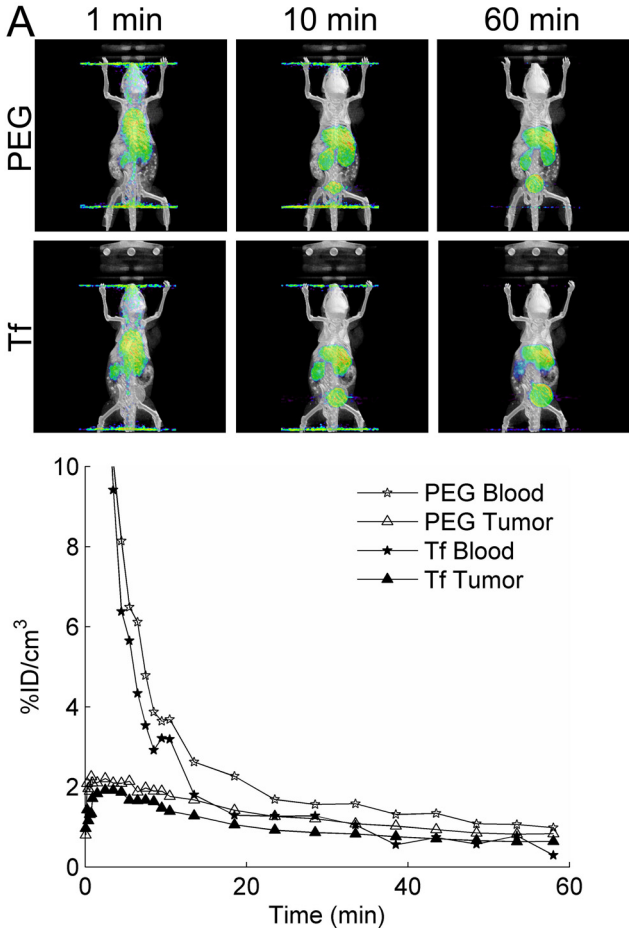


Figure 5.9. Tissue distribution of $^{64}$Cu-DOTA-siRNA delivered intravenously by Tf-targeted and non-targeted nanoparticles for the first 60 min after injection. (A) Fused microPET/CT images of mice at 1, 10, and 60 min after injection. (B) Blood clearance and tumor localization of Tf-targeted and non-targeted siRNA nanoparticles for the first 60 min after injection.

Figure 5.10 shows the microPET/CT images (1 d post injection) and corresponding bioluminescent images (pre injection and 1 d post injection) of two representative mice. The average tumor activity at 1 d post injection measured by microPET was 1.1±0.3 %ID/$cm^3$ and 1.4±0.4 %ID/$cm^3$ for Tf-targeted and non-targeted nanoparticles, respectively. Taking advantage of the noninvasive nature of the microPET/CT imaging, the same mice were also examined for luciferase activity by BLI before injection and 1 d post injection. The relative luciferase knockdown by the delivered siRNA molecules was calculated based on the percent change in the tumor luciferase activity (Figure 5.10C). The relative increase of tumor luciferase activity in mice treated with Tf-targeted nanoparticles is 50% lower than that in mice treated with non-targeted nanoparticles. This provides strong evidence suggesting that the Tf-targeted nanoparticles are able to deliver more functional siRNA to the tumor cells than non-targeted nanoparticles. These data also corroborate our observations showing that tumor growth inhibition by a therapeutic siRNA was only observed when the siRNA was delivered by Tf-targeted nanoparticles and not by non-targeted nanoparticles (6).

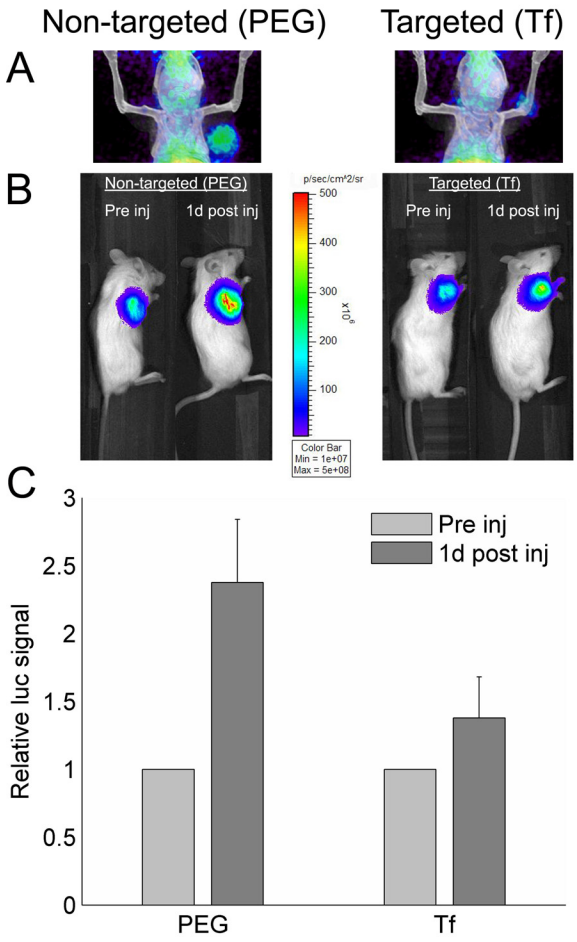


Figure 5.10. Multimodality in vivo imaging of siRNA nanoparticle delivery and function using microPET/CT and BLI. (A) Fused microPET/CT image showing tumor-associated activity 1 d post intravenous injection of Tf-targeted and non-targeted nanoparticles containing $^{64}$Cu-DOTA-siRNA. Image scale: min threshold = 0.1 %ID/cm$^3$, max threshold = 1.5 %ID/cm$^3$). (B) BLI of the same mice shown in (A) before injection and 1 d post injection. (C) Relative change in luciferase expression 1 d after intravenous injection of Tf-targeted (n = 7) and non-targeted (n = 4) nanoparticles containing $^{64}$Cu-DOTA-siRNA for simultaneous PET imaging. $p < 0.1$ based on a Student's t-Test with a two-tailed distribution.

## 5.5 Discussion

This study demonstrates the utility of noninvasive imaging technologies to concurrently examine the biodistribution and in vivo efficacy of siRNA nanoparticles. Synthesis of DOTA-conjugated siRNA molecules allowed labeling with $^{64}$Cu, a positron emitting radionuclide, and subsequent imaging by microPET. The spatiotemporal distribution of the injected $^{64}$Cu-labeled molecules was determined by co-registration of

the microPET images with anatomical information from microCT. The microPET technology allows collection of high resolution, three-dimensional biodistribution of the injected radiolabeled molecules over time. Therefore, the biodistribution of nanoparticles containing $^{64}$Cu-DOTA-siRNA could be followed after injection in living mice. Furthermore, because microPET/CT is noninvasive, BLI was used to measure the tumor luciferase activity in these same mice. By using an siRNA sequence that targets luciferase, the relative change in luciferase activity before and after injection serves as an indicator for siRNA function within the tumor cells.

The combination of microPET/CT and BLI represents a novel method to concurrently examine the biodistribution and functional efficacy of siRNA nanoparticle formulations in living subjects. Here, we used this methodology to investigate siRNA nanoparticles formed using cyclodextrin-containing polycations (CDP), as CDP has previously been shown to deliver functional siRNA to tumors in mice after systemic administration (6). Additionally, the CDP-based siRNA nanoparticles can be formulated with or without a Tf targeting ligand and can therefore be used to investigate the differences in biodistribution and functional efficacy of targeted and non-targeted nanoparticles.

DOTA-conjugated siRNA molecules targeting luciferase were synthesized by reacting DOTA-NHS with an siRNA containing a 5'-$NH_2$. The resulting DOTA-siRNA retained the ability to achieve luciferase knockdown in vitro, although the activity was reduced relative to the unmodified siRNA. Incorporation of DOTA-siRNA into the nanoparticles had negligible effects on the size and zeta potential of the resulting nanoparticles. Furthermore, nanoparticles containing 0%, 20%, and 50% DOTA-siRNA

all exhibited similar serum stability with an siRNA half-life of approximately 11 h in 50% mouse serum. Radiolabeling efficiencies of the DOTA-siRNA with $^{64}Cu$ were typically around 30-50%. These results all indicate that DOTA-modification of siRNA molecules has negligible impact on nanoparticle properties and is therefore a viable strategy for creating radiolabeled siRNA nanoparticles for imaging by microPET.

The results of the microPET studies indicated that attachment of the transferrin targeting ligand to the surface of the nanoparticles had negligible effect on the tissue distribution observed by PET. Both targeted and non-targeted nanoparticles demonstrated nearly identical tumor localization kinetics, and at 1 d post injection showed similar tumor accumulation representing ~1% ID/$cm^3$. This is likely due to the nonspecific tumor accumulation resulting from the enhanced permeability and retention (EPR) effect, which effectively traps large macromolecules in the tumor microenvironment regardless of cell-specific binding or internalization. However, BLI was used to examine function in tandem with the tissue distribution studies by microPET, and unlike the results with microPET showing that the tissue distribution was approximately equal for both targeted and non-targeted nanoparticles, BLI revealed that the targeted nanoparticles were more effective in reducing tumor luciferase expression 1 d post injection. Previous studies with other targeted delivery systems have also led to similar conclusions that the targeting moieties do not necessarily increase the total tumor accumulation but instead contribute to enhanced internalization by the tumor cells (17,18).

Even though the Tf-targeted nanoparticles were able to achieve luciferase knockdown after systemic administration, the biodistribution by microPET indicated that

a significant portion of the injected siRNA dose was rapidly cleared by kidney filtration. The possibility that the siRNA nanoparticles dissociate upon injection into the bloodstream led to investigation of a physiologically based mechanism to explain this observation. This effect may be most pronounced in the kidney since renal physiology provides a reasonable explanation for the observations made in this study and elsewhere concerning complexes formed by electrostatic interactions with nucleic acids. Even if the intact nanoparticles are not filtered through the glomerulus on account of their size, they still can travel through the nephron of the kidney via the vasa recta. Because of the countercurrent concentrating mechanism utilized by the kidney, NaCl concentrations in the vasa recta at the papillary tip of the renal medulla reach approximately 0.4 M (19). It is possible that the greatest dissociation of the nanoparticles takes place here, as the electrostatic interactions between the cationic polymer and the siRNA may be compromised in such high salt concentrations. The results in Figure 5.8 indicate ~50% dissociation of the siRNA nanoparticles at concentrations of 0.4 M. Additionally, once the free siRNA is released into the complex milieu of the blood, there is little chance for it to re-associate with the nanoparticles before being bound by other blood components or rapidly cleared by the kidney (through either glomerular filtration on the next pass or by active transport by transporters located on the renal proximal tubule cells).

Several previous studies have demonstrated that increasing amounts of NaCl can lead to concentration-dependent dissociation of complexes formed between nucleic acids and cationic polymers or lipids (20-22). Eldred et al. observed that complexes between lysine-based peptide oligomers and plasmid DNA showed a sharp rise in the amount of unpackaged DNA at ~550 mM NaCl (20). Additionally, Oupicky et al. examined NaCl-

mediated dissociation of DNA complexes formed with the cationic polymer, poly-L-lysine (21). They showed that when the polyplexes were crosslinked with DTBP (dimethyl-3,3'-dithiobispropionimidate), the polyplexes did not exhibit NaCl-dependent dissociation. Furthermore, while the non-crosslinked PEGylated polyplexes exhibited rapid clearance from the blood circulation, the crosslinked PEGylated polyplexes showed enhanced blood circulation times. These observations would be consistent with the hypothesized mechanism for disruption of the electrostatic nanoparticle interactions during blood circulation, particularly in the medulla of the kidney.

Further studies need to be conducted to confirm whether the conditions reached in the kidney medulla may be responsible for the disruption of the siRNA nanoparticles in this study. This disruption mechanism may have broad implications for the general design of nanoparticles assembled through electrostatic interactions. Although the siRNA nanoparticles used in this study were still able to deliver sufficient siRNA to achieve luciferase knockdown measured by BLI, the microPET experiments demonstrated that the majority of the injected dose was cleared rapidly from the blood circulation through kidney filtration. To achieve more efficient systemic delivery of siRNA through nanoparticle formulations, it will be imperative to address the short blood circulation times observed for the nanoparticle formulations. For nanoparticles formed through electrostatic interaction with nucleic acids, the increased salt concentration reached in the kidney (especially in juxtamedullary nephrons) may lead to significant nanoparticle dissociation and release of free nucleic acid. If the nanoparticles are stabilized against salt-induced dissociation, then they may begin to exhibit the desired property of extended circulation times, especially if the stabilized nanoparticles are

coated with a PEG layer to reduce interaction with cells in the reticuloendothelial system. Most likely an optimum stability will exist for the nanoparticle formulations that prevents excessive release of payload during circulation while still allowing adequate release upon cellular internalization.

## 5.6 Acknowledgments

The authors thank Dr. Waldemar Ladno, Dr. David Stout, Judy Edwards, Antonia Luu, and Amanda Armijo for assistance with microPET/CT imaging. The authors also thank Calando Pharmaceuticals for the gift of CDP, AD-PEG, and AD-PEG-Tf. DWB acknowledges the NSF for a Graduate Research Fellowship.

## 5.7 References


1. Soutschek, J., Akinc, A., Bramiage, B., Charisse, K., Constien, R., Donoghue, M., Elbashir, S., Geick, A., Hadwiger, P., Harborth, J. et al. (2004) Therapeutic silencing of an endogenous gene by systemic administration of modified siRNAs. *Nature*, **432,** 173-178.
2. Song, E., Zhu, P., Lee, S.-K., Chowdhury, D., Kussman, S., Dykxhoorn, D.M., Feng, Y., Palliser, D., Weiner, D.B., Shankar, P. et al. (2005) Antibody mediated in vivo delivery of small interfering RNAs via cell-surface receptors. *Nat Biotechnol*, **23,** 709-717.
3. Behlke, M.A. (2006) Progress towards in vivo use of siRNAs. *Mol Ther*, **13,** 644-670.
4. Zimmermann, T.S., Lee, A.C.H., Akinc, A., Bramlage, B., Bumcrot, D., Fedoruk, M.N., Harborth, J., Heyes, J.A., Jeffs, L.B., John, M. et al. (2006) RNAi-mediated gene silencing in non-human primates. *Nature*, **441,** 111-114.
5. Bartlett, D.W. and Davis, M.E. (2007) Physicochemical and biological characterization of targeted, nucleic acid-containing nanoparticles. *Bioconjugate Chem*, **18,** 456-468.
6. Hu-Lieskovan, S., Heidel, J.D., Bartlett, D.W., Davis, M.E. and Triche, T.J. (2005) Sequence-specific knockdown of EWS-FLI1 by targeted, nonviral delivery of small interfering RNA inhibits tumor growth in a murine model of Ewing's sarcoma. *Cancer Res*, **65,** 8984-8992.
7. Heidel, J.D., Yu, Z., Liu, J.Y.-C., Rele, S.M., Liang, Y., Zeidan, R.K., Kornbrust, D.J. and Davis, M.E. (2007) Administration in non-human primates of escalating intravenous doses of targeted nanoparticles containing ribonucleotide reductase subunit M2 siRNA. *P Natl Acad Sci USA*, **104,** 5715-5721.
8. Medarova, Z., Pham, W., Farrar, C., Petkova, V. and Moore, A. (2007) In vivo imaging of siRNA delivery and silencing in tumors. *Nat Med*, **13,** 372-377.
9. de Wolf, H.K., Snel, C.J., Verbaan, F.J., Schiffelers, R.M., Hennink, W.E. and Storm, G. (2007) Effect of cationic carriers on the pharmacokinetics and tumor localization of nucleic acids after intravenous administration. *Int J Pharm*, **331,** 167-175.
10. Bartlett, D.W. and Davis, M.E. (2006) Insights into the kinetics of siRNA-mediated gene silencing from live-cell and live-animal bioluminescent imaging. *Nucleic Acids Res*, **34,** 322-333.
11. Chow, P.L., Stout, D.B., Komisopoulou, E. and Chatziioannou, A.F. (2006) A method of image registration for small animal, multi-modality imaging. *Phys Med Biol*, **51,** 379-390.
12. Loening, A.M. and Gambhir, S.S. (2003) AMIDE: a free software tool for multimodality medical image analysis. *Mol Imaging*, **2,** 131-137.
13. Bartlett, D.W. and Davis, M.E. (2007) Effect of siRNA nuclease stability on the in vitro and in vivo kinetics of siRNA-mediated gene silencing. *Biotechnol Bioeng***,** in press.
14. Owen, J., Charles A. and Orvis, A.L. (1970) Release of copper by rat liver. *Am J Physiol*, **218,** 88-91.

15. van de Water, F.M., Boerman, O.C., Wouterse, A.C., Peters, J.G.P., Russel, F.G.M. and Masereeuw, R. (2006) Intravenously administered short interfering RNA accumulates in the kidney and selectively suppresses gene function in renal proximal tubules. *Drug Metab Dispos*, **34,** 1393-1397.
16. Braasch, D.A., Paroo, Z., Constantinescu, A., Ren, G., Oz, O.K., Mason, R.P. and Corey, D.R. (2004) Biodistribution of phosphodiester and phosphorothioate siRNA. *Bioorgan Med Chem*, **14,** 1139-1143.
17. Maeda, N., Miyazawa, S., Shimizu, K., Asai, T., Yonezawa, S., Kitazawa, S., Namba, Y., Tsukada, H. and Oku, N. (2006) Enhancement of anticancer activity in antineovascular therapy is based on the intratumoral distribution of the active targeting carrier for anticancer drugs. *Biol Pharm Bull*, **29,** 1936-1940.
18. Kirpotin, D.B., Drummond, D.C., Shao, Y., Shalaby, M.R., Hong, K., Nielsen, U.B., Marks, J.D., Benz, C.C. and Park, J.W. (2006) Antibody targeting of long-circulating lipidic nanoparticles does not increase tumor localization but does increase internalization in animal models. *Cancer Res*, **66,** 6732-6740.
19. Edwards, A., Delong, M.J. and Pallone, T.L. (2000) Interstitial water and solute recovery by inner medullary vasa recta. *Am J Physiol Renal Physiol*, **278,** F257-F269.
20. Eldred, S.E., Pancost, M.R., Otte, K.M., Rozema, D., Stahl, S.S. and Gellman, S.H. (2005) Effects of side chain configuration and backbone spacing on the gene delivery properties of lysine-derived cationic polymers. *Bioconjugate Chem*, **16,** 694-699.
21. Oupicky, D., Carlisle, R. and Seymour, L. (2001) Triggered intracellular activation of disulfide crosslinked polyelectrolyte gene delivery complexes with extended systemic circulation in vivo. *Gene Ther*, **8,** 713-724.
22. Pozharski, E. and MacDonald, R.C. (2003) Lipoplex thermodynamics: determination of DNA-cationic lipid interaction energies. *Biophys J*, **85,** 3969-3978.